

# Verification of compaction and rarefaction models for fused silica with 40 billion pulses of 193-nm excimer laser exposure and their effects on projection lens imaging performance

J. Martin Algots<sup>\*a</sup>, Richard Sandstrom<sup>a</sup>, William Partlo<sup>a</sup>,  
Kazuhiro Takahashi<sup>b</sup>, Hiroyuki Ishii<sup>b</sup>, Yasuo Hasegawa<sup>b</sup>;

<sup>a</sup>Cymer, Inc., 17075 Thornmint Ct, San Diego, CA, USA 92127;

<sup>b</sup>Canon, Inc., 23-10, Kiyohara-kogyo-danchi, Utsunomiya-shi, Tochigi-ken, 321-231, Japan.

## ABSTRACT

Extensive testing of fused silica has been completed over the past few years by several researchers. A generalized model has been proposed that describes both the compaction that occurs at high peak intensities and the rarefaction that occurs at lower peak intensities. An exposure setup has been constructed to help verify these damage models and to determine the fitting parameters for various types and processing of fused silica. This setup simultaneously exposes samples to two sets of intensities, each set with a different integrated-square pulse width. To make these tests relevant to the microlithography community, the energy densities chosen for these tests span the range found in the projection optics of a 193nm excimer laser-based microlithography tool ( $50\mu\text{J}/\text{cm}^2$  -  $400\mu\text{J}/\text{cm}^2$ ). The samples have been exposed for 40 billion pulses with wavefront measurements made periodically with both 633nm interferometry and 193nm interferometry. This large number of pulses represents the equivalent of several years worth of lens exposure. Data for several fused silica samples will be presented and comparisons will be made to the proposed damage model. According to the obtained parameters, optical performance will be estimated during long term laser exposure on the projection optics. We take into consideration actual light intensity on each lens element for several illumination conditions. We will discuss the difference of the impact on optical performance between different fused silica materials, illumination conditions, reticle transmission, pulse durations, number of pulses, and so on.

**Keywords:** Lithography, Excimer, ArF, Fused Silica, Compaction, Rarefaction, Pulse Stretch.

## 1. INTRODUCTION

Fused silica is currently the most widely used lens material in the manufacture of 193 nm (ArF) microlithography lenses. These lenses are composed of 20-30 elements and represent a significant portion of the cost of a stepper or scanner. They must maintain very stringent imaging qualities to assure high yields of the wafers that they expose. As the technology roadmaps continue to demand smaller features, the resolution requirements get even more stringent.

The fused silica material is not completely stable under 193 nm irradiation, however. During exposure the index of refraction of the material can change. Both increases and decreases in the index of refraction are observed, depending on the energy density, number of laser pulses and the specific materials being tested. To allow the lens designers to predict the performance of their lens designs over the life of the lens, a model has been proposed to predict these changes. The model breaks the changes in refractive index into two components, one accounts for an increase in the index and the other a decrease. Both components can be present in the same sample.

Once a model is determined for a material it can be incorporated into a simulation of the performance of a lens design. The spatial optical load of each lens element is estimated based on the number and type of reticles used and the illumination scheme used for those wafer layers. Based on these exposures the change in index of refraction for the lens element is determined. The results are put back into the lens design program and compared to the design performance without these long term exposure effects.

---

\* malgots@cymer.com; phone 858/385-5241

This paper reports on the measured effects of exposing fused silica samples to 40 billion pulses of 193 nm radiation and how they will affect the performance of a 193 nm scanner lens lifetime.

## 2. TEST SET UP

### 2.1. Laser configuration

For this experiment, a modified Cymer Nanolith 7000 laser was used. Modifications included broadband operation ( $\sim 0.5$  nm FWHM) and prototype modules to allow 100% duty cycle operation at 4000 Hz and higher pulse energies than standard, line narrowed lasers.

The laser cavity was built with partial reflectors of 30% on both ends with apertures on both ends of the cavity of 2.6(w) x 12.5(h) mm (Figure 1). Outboard of each partial reflector was an anamorphic beam expander that widened the beam 4X. The left hand beam was reflected around the back of the laser to the test chamber with two 45° full reflectors. This beam had an average  $t_{is}$  pulse length of approximately 18 nsec.

The right hand beam was run through an optical pulse stretcher. The pulse stretcher was a re-imaging time delay loop consisting of a beam splitter and four concave mirrors creating a confocal resonator. The delay was 22 nsec and the overall efficiency was approximately 85-90%. The  $t_{is}$  pulse length of the stretched pulse was approximately 45 nsec. Typical stretched and non-stretched temporal profiles are shown in Figure 2.

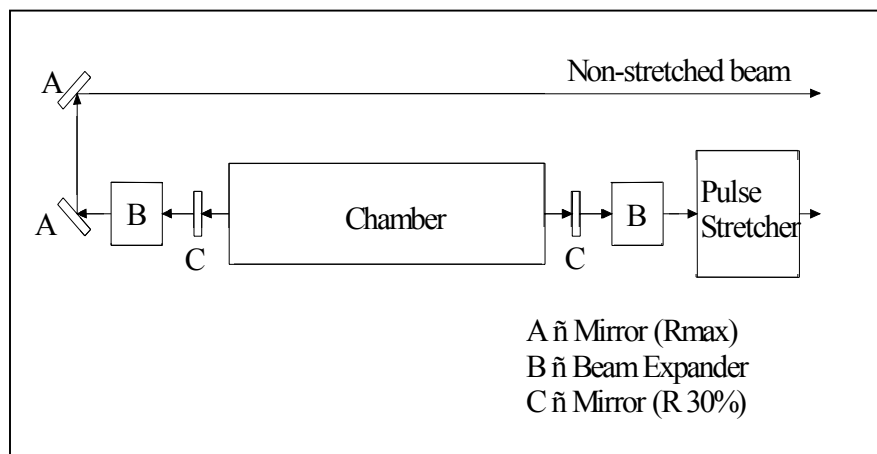


Figure 1. Laser Configuration, Top View

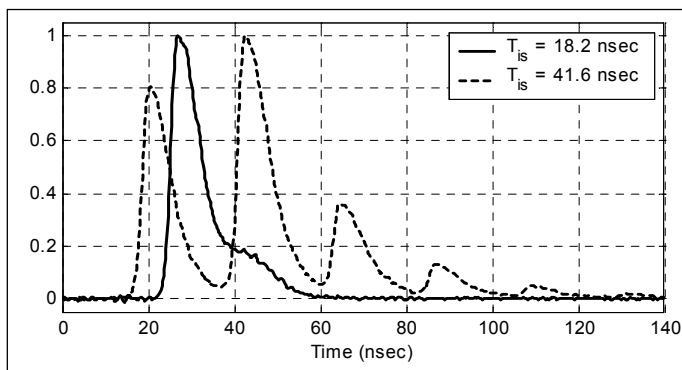


Figure 2. Typical Normalized Pulse Shape

### 2.2. Test configuration

The experiment was run on a 12 x 4 foot optical table covered with a custom aluminum enclosure with glass windows. The enclosure was purged with nitrogen and oxygen levels were measured and maintained below 10 ppm.

Three separate beam lines were created. Each beam line exposed 6 samples, single pass, in a serial arrangement. The beam line consisted of 4 intensities of both stretched and non-stretched pulses.

Both stretched and non-stretched beams entered the table and were individually rotated and turned 90° with two mirrors (forming a periscope), giving a beam size of 6mm high x 13 mm wide. As each beam traveled across the width of the table, it was then split into three beams, one for each of the three beam lines and directed down the length of the table. The non-stretched beams were directed parallel to and 10 mm above the stretched beams, making up the beam line. Each beam line was then subjected to its own  $\Omega$  wave plate and anamorphic beam expander to widen the beam.

Following the beam expanders in each beam line were two attenuators, one directly over the other (six total), that allowed independent control of the stretched and non-stretched components of the beam lines. To create multiple energy densities, each beam line was subjected to multiple fused silica plates (stacked attenuators) that, using Fresnel reflection, attenuate the beam line to form 4 equal steps across the width of the beam line resulting in full, one-half, one-quarter and one-eighth energy densities. Finally, each beam line went through a  $^{\circ}$  waveplate for rotational polarization and then a 2 x 4 array of  $\phi 5$  mm apertures before the first sample.

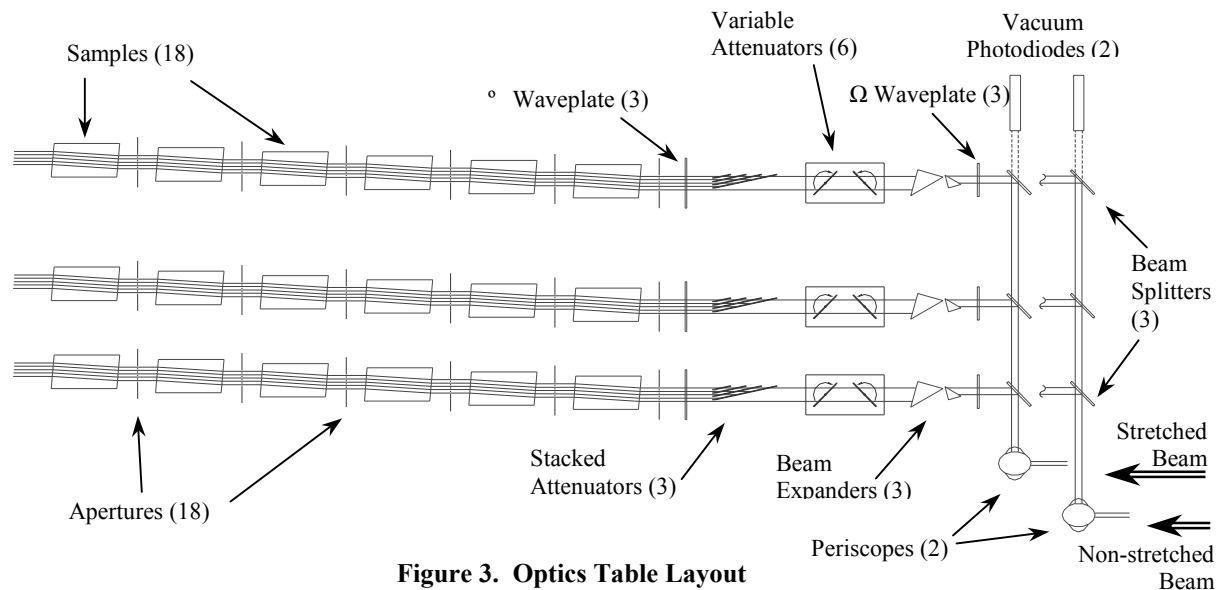


**Figure 3. Optics Table Layout**

Each of the three beam lines illuminated 6 samples in series, single pass. The samples were mounted on translation stages, such that they could be moved in and out (perpendicular to) the beams. Behind each of the first five samples in each beam line was an additional aperture, of the same geometry as the first, which cleans up the beam before it reached the next sample. These inter-sample apertures were on computer-controlled actuators that allowed the apertures to be flipped out of the beam path during the insitu measurement process.

### 2.3. Exposure Protocol

The samples measured 50 mm wide x 25 mm high x 100 mm long. The ends of the samples were cut and polished at  $2^{\circ}$  from perpendicular to control Fresnel reflections. The samples were exposed through the 100 mm length. Each sample was exposed with one beam line, consisting of eight beams, two rows of four beams each (see Figure 4). The four top beams were from the non-stretched side of the laser and the four bottom beams were from the stretched. Each beam delivered  $\Omega$  as much pulse energy as the previous, so that nominal energy densities of 400, 200, 100 and 50  $\mu\text{J}/\text{cm}^2$  were achieved on the same sample at the same time.

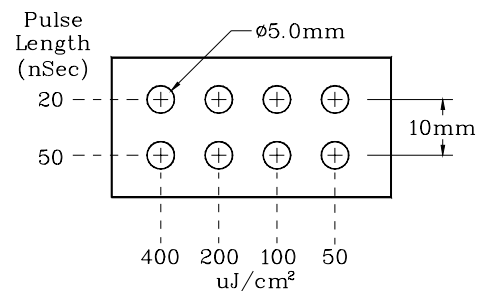


**Figure 4. Illumination of Sample.**

With six samples illuminated in series, the Fresnel reflections of each surface reduced the energy density on each downstream sample. To reduce the build up of reflections in the samples, apertures were installed between each sample to clean up the beam and block most of the reflections from samples further down stream.

## **2.4. Insitu Metrology**

A CCD camera and power meter were used to measure the energy densities incident on and transmitted through each sample. The camera and power meter head were mounted on an X-Y stage allowing them to be positioned before and after each sample. Three CCD images for each sample were taken, one for the four right most exposure spots, one for the center exposure spots and the last for the four left most exposure spots, the center four exposure spots thus get imaged twice. This automated measurement routine was executed twice a day, once before refilling the laser chamber with fresh gas and once after the new gas had warmed up.

Two Hamamatsu vacuum photo diodes were used to measure the temporal pulse shape. The signals from the diodes were recorded on an oscilloscope and then downloaded and processed with a LabView program. This measurement was made every 15 minutes during exposure. The oxygen level in the test enclosure was monitored continuously and was recorded every 15 minutes.

## **2.5. Exsitu Metrology**

Every 2.5 billion pulses the samples were taken out of the test enclosure and measured with a 633 nm Zygo interferometer. The interferometer was enclosed in a covered, floating table and dedicated to this experiment. Computer controlled stages were used to manipulate the samples to reduce thermal disturbances. Four wavefronts were taken of each sample as well as four reference wavefronts.

At 15, 20, 25, and 40 billion pulses the samples were sent to a third party to be measured on a custom built 193 nm interferometer.

# **3. DATA ANALYSIS**

## **3.1. 633 nm Interferometry**

To minimize the noise in the interferometry, four measurements were made of each sample with four associated reference measurements (measurements without the sample in place). The average of the reference wavefronts was subtracted from the average of the sample wavefronts. For each exposure level, the zero pulse wavefront was then subtracted from the wavefront of the exposed sample to remove the curvature of the sample itself. Finally piston, xy slope, xy cylinder, twist,  $x^3$ , and  $y^3$  were calculated after masking out the exposed regions and subtracted from the wavefront, creating a final wavefront.

The final processed wavefronts are then filtered with a spot meter filter. This filter averages the circular area of the exposed region and subtracts from it the average of an annulus around the exposed region. The diameter of the averaged circle was 0.75x the diameter of the exposed region and the annulus had inside and outside diameters of 1.25x and 1.5x the exposed region diameter, respectively. The filtered wavefront is then scanned in each of the eight exposure areas for the maximum value of each area. These values are the average wavefront change of the sample for the measurement.

The accuracy of this spot meter method of measuring the change in optical path length of the samples was determined to be approximately 1 nm. Converting to index of refraction, the accuracy implies a measurement of 10 ppb.

## **3.2. 193 nm Interferometry**

The 193 nm wavefronts were analyzed with the same spot meter filter. Averaging and reference subtraction was done by the third party that made the measurements. The accuracy of the 193 nm measurements suffered for several reasons. Measurements before exposure were not available and could not be subtracted from the exposed wavefront images. The equipment could not be dedicated to this experiment and imaging quality varied from measurement to measurement.

### 3.3. Illumination Calculations

For each automated measurement sequence, three CCD images recorded the incident radiation on each sample. Each image captured four exposure regions, the four middle regions being captured twice. The images were stitched together, averaging those regions that were imaged twice and scaling subsequent images by the overlapping regions. The composite image was then calibrated to the power meter readings for that sample resulting in a spatial energy density map.

## 4. ANALYSIS OF 633 nm DATA

As with the prior results<sup>1</sup>, the samples fall into three classes of behavior; compaction dominated, rarefaction dominated, and balanced between compaction and rarefaction. The results for sample A, shown in Figure 5, are typical of samples where rarefaction dominates the refractive index change.

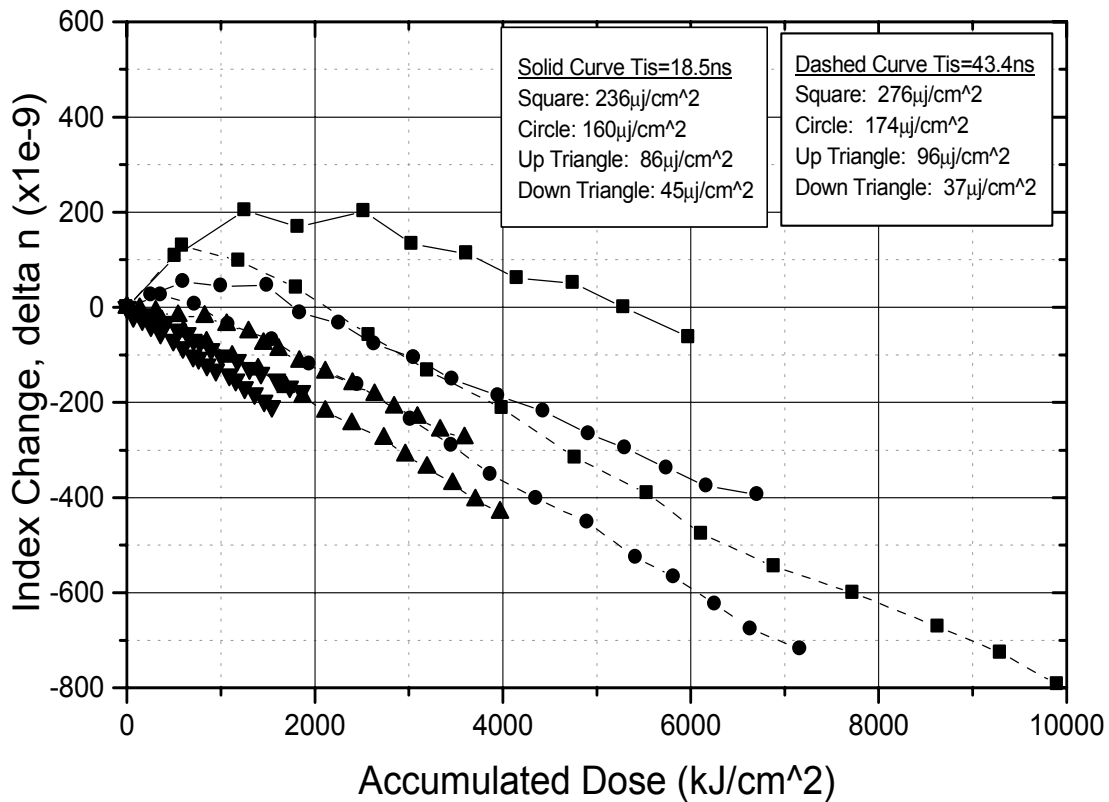


**Figure 5. Measured refractive index change vs. accumulated dose for a rarefaction dominated sample of fused silica.**

The index change model described previously<sup>1</sup> includes terms for compaction and rarefaction, with the rarefaction term possessing an exponential saturation term and the compaction term following the square law in energy density, as showed below.

$$\partial n = \Delta n_{\text{sat}} \left( 1 - e^{-\frac{NI}{D_o}} \right) + \left( k_2 \frac{NI^2}{t_{\text{is}}} \right)^b.$$

The results after 10 billion pulses showed that the saturation dose for the exponent in the rarefaction term was very large and thus the data up to 10 billion pulses could be modeled equally well with a simple linear term for the rarefaction.

$$\partial n = \frac{\Delta n_{\text{sat}}}{D_0} (NI) + \left( k_2 \frac{NI^2}{t_{\text{is}}} \right)^b .$$

For the measured data out to 40 billion pulses, a simple linear function for the rarefaction term no longer satisfactorily describes the amount of index change for the high energy density exposures. On the other hand, the exponential fit, though effective at describing the index change over a wide range of energy density values, leads to considerable calculation overhead when performing a full projection lens simulation. A compromise can be made between goodness of fit and calculation speed using a model of the form:

$$\partial n = k_1 (NI)^a + \left( k_2 \frac{NI^2}{t_{\text{is}}} \right)^b ;$$

where N is the number of pulses, I is the incident energy density (mj/cm<sup>2</sup>), t<sub>is</sub> is the integral square pulse duration<sup>2</sup> (ns), and k<sub>1</sub>, k<sub>2</sub>, a, and b are fitting parameters. In order to ease the calculation requirements for projection lens simulations, described in a later section, we will perform the data fitting using this compromise model.

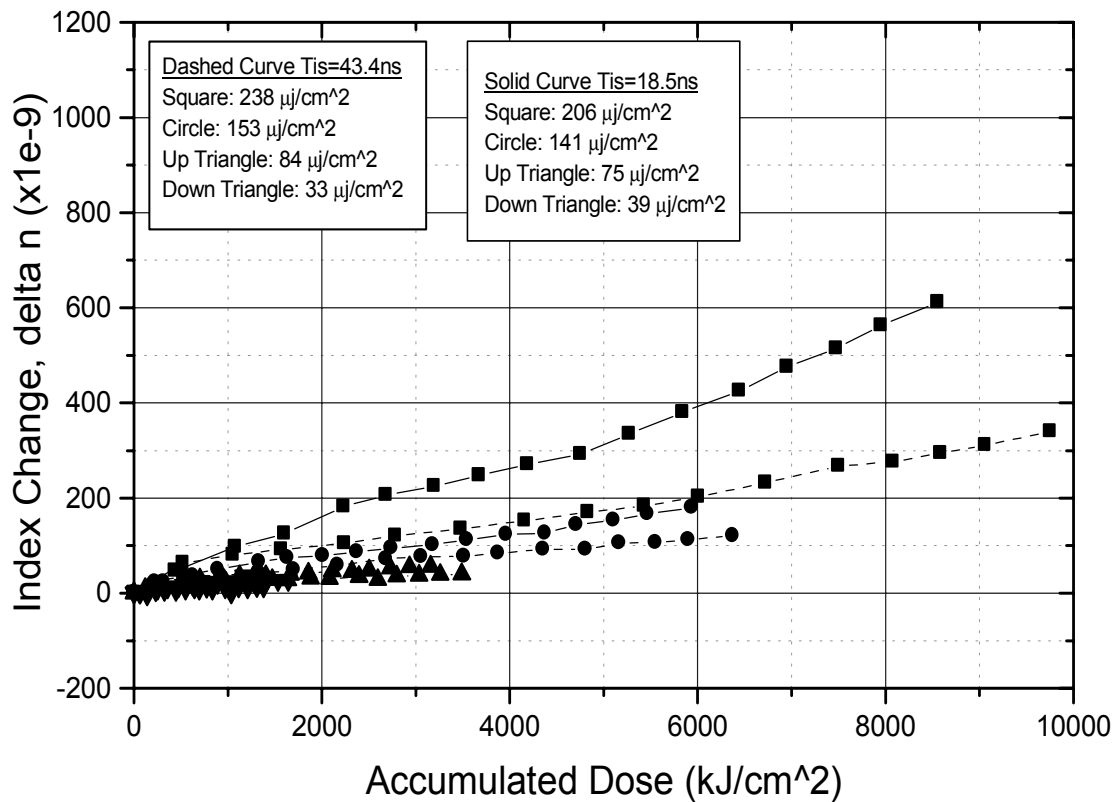
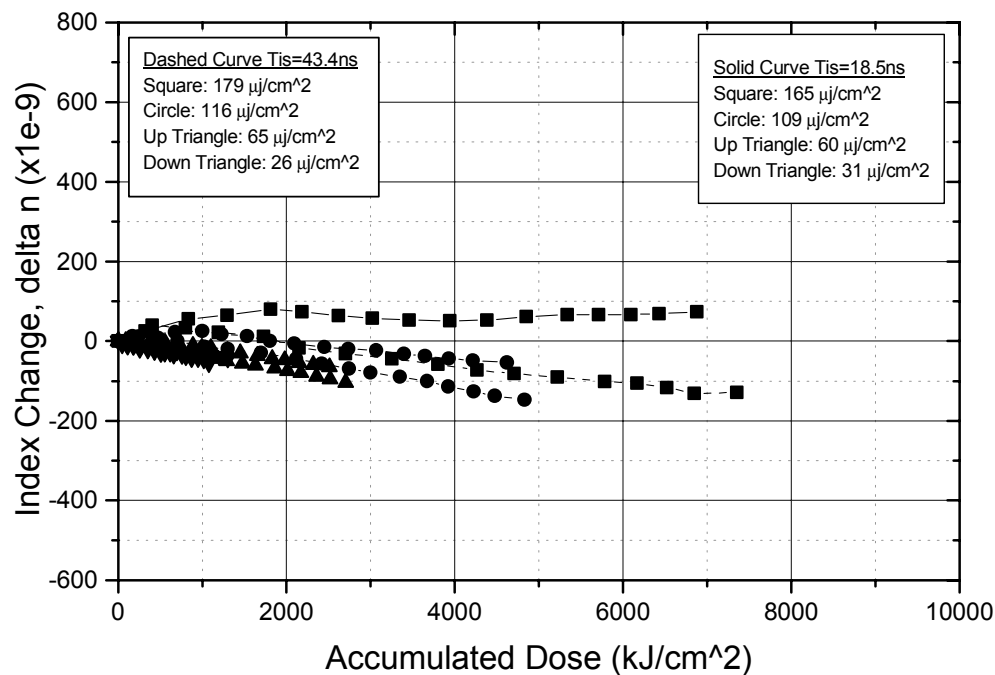


Figure 6. Measured refractive index change vs. accumulated dose for a compaction dominated sample of fused silica, sample B.

For the example of a rarefaction dominated sample shown in the Figure 5, the wavefront change is in the negative direction and is nearly linear with accumulated exposure except for the highest values of energy density. In this case, the fitted values for the  $k_1$  and  $a$  coefficients are such that the first term in the model dominates. Note that for all exposures except those with the largest values of intensity there is little or no dependence on pulse duration.

For the case of a compaction dominated material like sample B shown in Figure 6, the fitted value of  $k_1$  is very small and thus the second term in the model dominates the predicted index change. The dependence on pulse duration is evident in the fact that the exposures with longer pulse duration, but with similar energy density, lead to a smaller index



**Figure 7. Measured refractive index change vs. accumulated dose for a balanced sample of fused silica, sample C.**

change.

The final class of material type is that which exhibits a balance between compaction and rarefaction effects. Sample C, with its data shown in Figure 7, is one such example. In this case the total index change with exposure is small for all accumulated dose values. There is some dependence on pulse duration as can be seen by the fact that the index change for the highest intensity is positive for a short pulse duration and negative for a long pulse duration. The fitted values for  $k_1$  and  $k_2$  are such that neither term in the model dominates the predicated index change.

The fitted values for each of the three types of material are shown in the table below for comparison. The fitting constraints where:  $B \leq 1$ ,  $K_1 \leq 0$ , and  $K_2 > 0$ .

	Sample A	Sample B	Sample C
$K_1 \left( \frac{J}{\text{cm}^2} \right)^{-1}$	-0.051	0.00	-0.109
a (unitless)	1.1	n/a	0.83
$K_2 \left( \frac{J^2}{\text{cm}^4 \text{ns}} \right)^{-1}$	12.1	5.24	2.82
b (unitless)	0.98	1.0	1.0

**Table 1. Model parameters for 633 nm**

The resulting b coefficients upon fitting to the 40 billion pulse data set were unexpected since the fitting results for the 10 billion pulse data set resulted in b coefficients close to 0.6 (sample A: b=0.58, sample B: b=0.66, sample C: b=0.37 for the 10 billion pulse data). As more dosage was accumulated during these tests, the measured index variation curves began to lose their square-root shape and began to appear more linear. We have no physical explanation for this behavior, but it may have important consequences if a lens lifetime prediction depends on the saturation character of a square-root law index change.

## 5. ANALYSIS OF 193 nm DATA

The 193 nm data for analysis is rather limited. First of all, the usable measurements were only made at 4 points during the test, at 15, 20, 25 and 40 billion pulses. Secondly, of those four measurements, some of the exposure regions had so much wavefront deformation that they could not be successfully measured with the available interferometer. In addition, unlike the 633 nm interferometer, the 193 interferometer could not be dedicated to this test, so fixturing had to be set up each time a measurement was made, which contributed to the noise of the measurements.

The 193 nm data was fit to the same model that the 633 nm data was. Solving for the 4 parameters ( $k_1$ ,  $k_2$ , a and b) turned out to be somewhat subjective, as the optimization space for the parameters exhibited a large flat minimum area (Figure 8).

For sample A the minimum fell at  $k_1 = -0.051$ ,  $k_2 = 37.6$ ,  $a = 1.14$  and  $b = 0.76$ . Since a is greater than 1.0 this would indicate that the rarefaction term of the data has not started to saturate yet, but the compaction term has started to saturate. Though this model does fit the data reasonably well (Figure 9), as the exposure continues and the rarefaction starts to saturate, the model will likely not hold and new exponents and coefficients will need to be calculated.

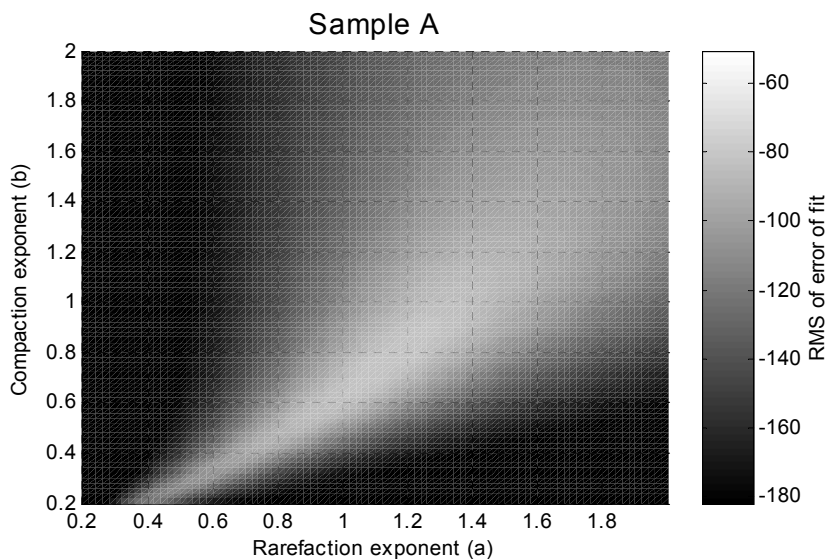


**Figure 8. Sample A fit to model, RMS of error of fit**



For sample B the minimum fell at  $k_1 = -0.026$ ,  $k_2 = 8.09$ ,  $a = 0.27$  and  $b = 0.97$ . Since the rarefaction of this material is almost non-existent,  $k_1$  can be set to 0.0 making  $a$  arbitrary and leaving the optimization of  $k_2$  and  $b$ .

The solution for sample C is at  $a = 3.00$  and  $b = 1.98$  with  $k_1$  nearly 0.0. This does not make any physical sense (the compaction can't continue growing exponentially), so limiting the exponents to 1.0 results in a solution at  $k_1 = -0.101$ ,  $k_2 = 38.6$ ,  $a = 1.00$  and  $b = 0.74$ .

Since there is a possible physical explanation for choosing a compaction exponent of 0.667, the models of samples A and C were calculated for  $b = 0.667$  for both 633 and 193 data so a comparison of  $k_2$  could be made. A solution of this form was not successful for sample B, so it was left at  $b = 1.00$ .

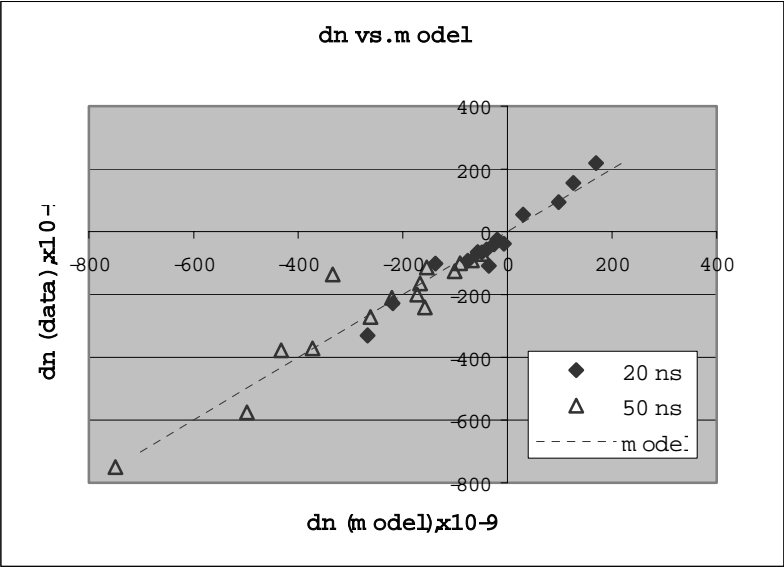


Figure 9. Fit of data to model for sample A, 193 nm wavefront deformation.

		Sample A	Sample B	Sample C
193 nm	$k_1$	-0.182	0.0	-0.110
	$a$	1.00	n/a	1.00
	$k_2$	421	7.64	390
	$b$	0.667	1.00	0.667
633 nm	$k_1$	-0.325	0.0	-0.237
	$a$	0.917	n/a	0.839
	$k_2$	277	5.52	136

Table 2. Model parameters for 193 nm.

For all three samples, the change in index of refraction is greater for the 193 nm measurements compared to the 633 nm measurements. This agrees with Moll<sup>3</sup> that a photorefractive component exists that produces a higher index of refraction at 193 nm than 633 nm. This reveals itself in Table 2 as higher  $k_2$  values for all three samples. In fact both samples A and C could be seen to compact when measured at 193 nm and the same exposure region would show to be rarefacting at 633 nm.

## 6. ESTIMATION ON PROJECTION LENS

### 6.1. Simulation conditions

In this chapter, we estimate the effects of compaction and rarefaction of fused silica on the optical performance of projection optics. The calculation goes as follows. First, we fit the laser exposure induced refractive index change measured with the 193 nm interferometer introduced in the previous chapter with a linear approximation model and calculate the parameters of  $k_1$ ,  $k_2$ ,  $a$  and  $b$ . Then we determine wafer layers processed with an ArF tool and assume

illuminator conditions, appropriate dose and reticle transmittance toward the typical logic and memory device for estimating the effects of long-term use. Table 3 shows an example of the conditions. In this paper, the optical performance of the projection optics after seven years worth of exposure is estimated. Assuming an annual usage of 10 billion pulses and that the ratio of actual effective incident pulses to the lens is estimated at about 75%, then the change after 50 billion pulses exposure is calculated. The number of pulses in seven years for each layer are determined from the number of layers and resist sensitivity of each layer in Table 3. Laser pulse width is assumed to have a  $t_{is}$  of 50 nsec.

Device	Layer	Illumination	Number of layers	Reticle transmission	Resist Sensitivity
Logic	Isolation	Conventional	1	90%	300J/m <sup>2</sup>
	Gate	Small $\sigma$	1	90%	300J/m <sup>2</sup>
	Gate -trim	Annular	1	50%	300J/m <sup>2</sup>
	Contact	Conventional	1	10%	550J/m <sup>2</sup>
	Local Metal	Annular	1	50%	300J/m <sup>2</sup>
	Local Via	Conventional	1	10%	550J/m <sup>2</sup>
	Mid Metal	Annular	5	40%	300J/m <sup>2</sup>
	Mid Via	Conventional	5	10%	550J/m <sup>2</sup>
Memory	Isolation	Annular	1	50%	300J/m <sup>2</sup>
	Gate	Dipole	1	70%	300J/m <sup>2</sup>
	Bit Contact	Conventional	1	15%	550J/m <sup>2</sup>
	SN Contact	Conventional	1	30%	550J/m <sup>2</sup>
	Capacitor	Conventional	1	60%	300J/m <sup>2</sup>
	Local Metal	Dipole	2	60%	300J/m <sup>2</sup>
	Via	Conventional	1	15%	550J/m <sup>2</sup>

Table 3. Estimation Layer Model

### 6.2. Calculation for lens element

We now calculate the distribution of energy density for each lens element. The illuminator gives light through the slit by the layer-dependent illumination condition listed in Table 3, into the lens element, divided into a 255 x 255 element mesh, and use a ray trace to calculate the energy density of the mesh for each lens element. The amount of energy is

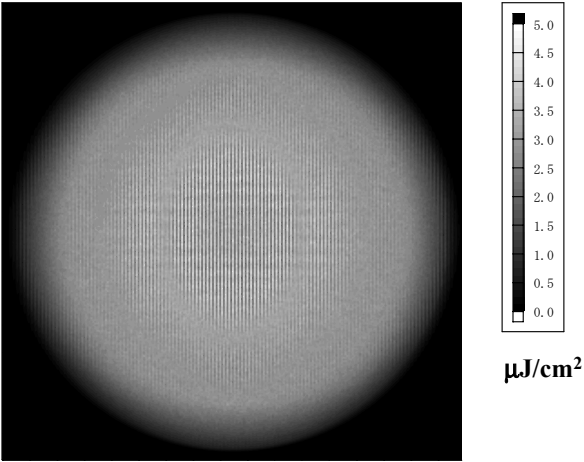


Figure 10. Energy density distribution on a lens element

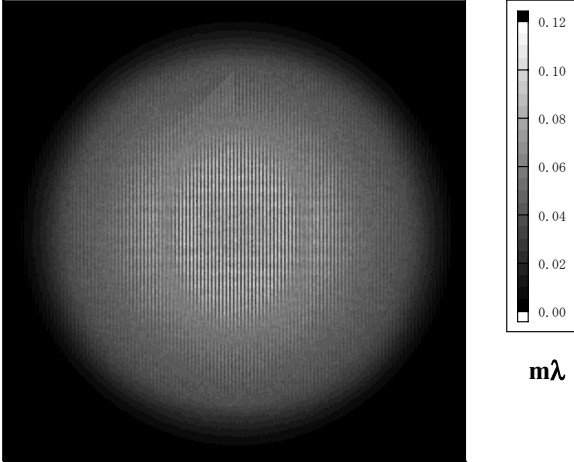


Figure 11. Wavefront aberration change caused by compaction and rarefaction on a lens element

determined by the intensity at the reticle plane and the reticle transmittance. This distribution contains only 0th order illumination, no diffraction beams at the reticle pattern are taken into the account, which means that the estimation here is done at the most severe case. In an actual lens, the distribution of the energy density is more uniform due to the diffraction from the reticle pattern, thus making the actual value smaller than the modeled value. Figure 10 shows a calculated result of the distribution of the energy density with 0th order illumination on a lens element.

Once the energy density distribution is determined, the distribution of refractive index change for each lens element is calculated by using the model equation and the number of pulses for each layer defined from conditions in Table 3. In addition, the wavefront aberration change at the lens is calculated by considering the light path length in the lens. An example of the result is shown in Figure 11.

The wavefront aberration change from each layer is obtained by repeating this calculation on every lens element and summing all the wavefront aberration changes. It is possible to estimate the wavefront aberration change caused by refractive index change of the fused silica after continuous production of logic or memory devices for seven years by performing the above to the all layers.

### 6.3. Results

Using the above-mentioned simulation procedure, we evaluate the effect on a projection lens when all fused silica lenses are made of rarefaction dominated materials (sample A), compaction dominated material (sample B) and balanced material (sample C). The RMS of the wavefront aberration, which changes over seven years use, is taken as the evaluation criterion. The results are shown in Figure 12. Sample B (compaction dominated material) shows the least change on both logic and memory devices. Sample A (rarefaction dominated material) shows the biggest change. Figure 13 compares the change of layers using material B as an example. Among the layers of logic devices, the change on the

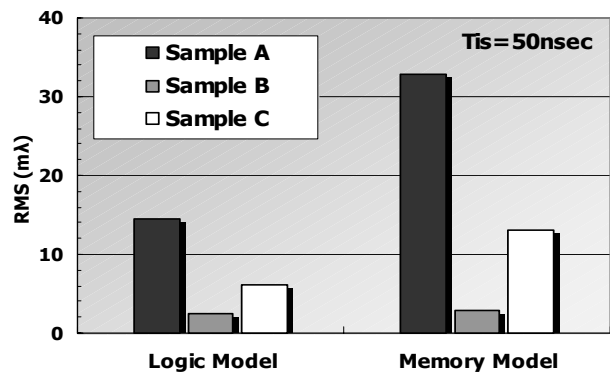


Figure 12. Wavefront aberration change after 50Bpls exposure with Tis=50nsec (7 years)

gate layer is biggest, because the transmittance is assumed to be large at 90%, and the energy density in the lens is higher at a small sigma setting compared to other illuminator conditions. For the memory devices, the transition on the gate layer and the local metal process is large. The local metal process needs two layers because of the use of dipole illumination. The transmittance on both layers is relatively high and both dipole illumination and small sigma values cause high energy densities.

The RMS of the wavefront aberration change after seven years of use is 5 mλ or less for both devices in the case of material B, despite the worst case calculation. We consider only 0th order illumination, neglecting diffraction effects of the reticle, and assume high reticle transmittance. Therefore the result of the simulation is more severe than actual operating conditions, indicating that no practical problems are expected. By comparison, when the lens consists of either material A only or material C only, the aberration drift is larger, thus it may become a problem under certain operation conditions.

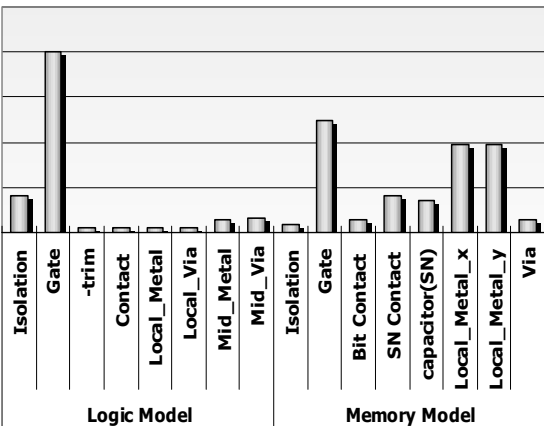


Figure 13. Wavefront aberration change for each layer

#### 6.4. Discussion

To examine the effect of laser pulse width, the transition of wavefront aberration is calculated with a  $t_{is}$  of 20 nsec (Figure 14). In comparison to a  $t_{is}$  of 50 nsec, the value of sample B (compaction dominated material) deteriorates, sample C shows no difference, and sample A shows some improvement.

Because  $t_{is}$  is in the numerator of the compaction term of the model for refractive index change, a longer  $t_{is}$  makes the change smaller in the case of compaction dominated materials. On the contrary, for rarefaction dominant materials, because an increase in the compaction term can cancel the rarefaction term, reducing the total index of refraction gradient, a smaller  $t_{is}$  gives better results.

In the energy density range of this sample test, the balanced material of sample C shows the smallest change in refractive index. In the case of an actual projection lens, however, compaction dominated material (sample B) produces a smaller change in the wavefront aberration. This shows that the result depends on which energy density range dominates in the actual lens. The energy density histogram of a fused silica lens with the illuminator condition of  $\sigma = 0.25$  is shown in Figure 15. One point corresponds to one mesh element on the lens surface. The graph shows that almost all points are smaller than  $50 \mu\text{J}/\text{cm}^2$ , and it is possible to make the change of wavefront aberration smaller by using material B, which shows the smallest refractive index change in this energy density range.

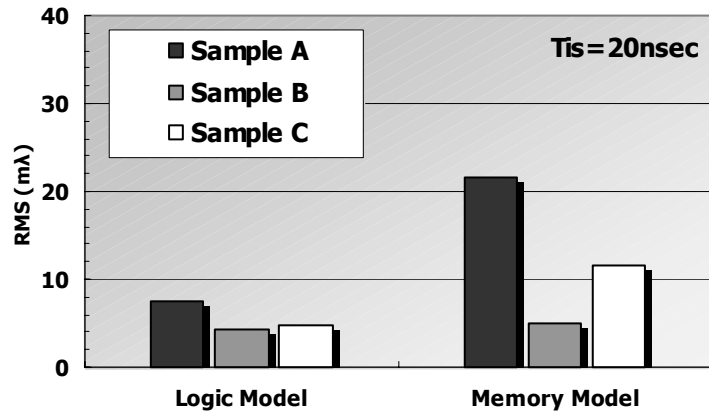


Figure 14. Wavefront aberration change after 50Bpls exposure with  $T_{is}=20\text{nsec}$  (7 years)

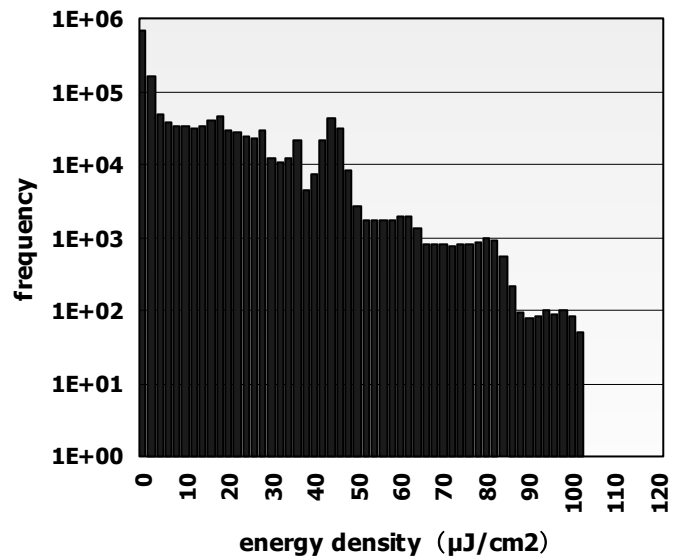


Figure 15. Histogram of energy density distribution in projection optics.

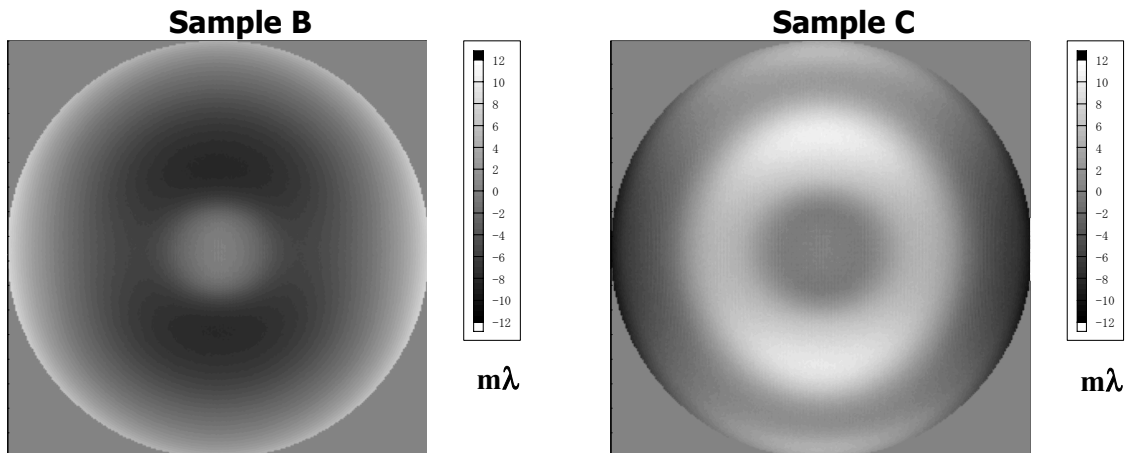


Figure 16. Comparison of total wavefront aberration changes in two different samples

As a result of our test, the required performance of fused silica, in terms of laser durability, is small refractive index change in energy densities under  $50\mu\text{J}/\text{cm}^2$ . In addition, compaction dominated material is desirable from the aspect of its ability to improve the durability by extending the pulse length.

Figure 16 shows the comparison of wavefront aberration change in the case of using fused silica materials B and C. The directions of wavefront aberration change are opposite. It is therefore possible to reduce the change of wavefront aberration less than the change shown in Figure 12 by selectively combining compaction dominant materials and rarefaction dominant materials in the actual lens design.

## 7. CONCLUSIONS

This study introduces a method of evaluation for projection lens optical performance by using the linear model approximation obtained from the result of endurance test on fused silica. We prove that there is no problem with the durability of ArF projection lens within the level of fused silica sample used in this test. Required capability to fused silica in terms of durability is small value in refractive index change in energy density under  $50\mu\text{J}/\text{cm}^2$ , and compaction dominated materials are desirable.

## 8. ACKNOWLEDGEMENTS

The authors would like to thank Eiichi Murakami and Hidenori Hashiguchi of Canon Inc. for their cooperation with preparing this paper and Michael Lysik, Kevin Duenow and Todd Embree for their help in running and maintaining the test.

## References

1. J.M Algots, et al, "Compaction and Rarefaction of Fused Silica with 193-nm Excimer Laser Exposure," *Proc SPIE* **5040**, pp 1639-1650, 2003.
2. R. Sandstrom, *Proc of 2nd Symposium on 193nm Lithography*, Colorado Springs, CO, 1997.
3. J. Moll, P. Dewa, "Laser resistance of fused silica for microlithography: experiments and models", Corning, Inc., [http://www.corning.com/discovery\\_center/science\\_\\_technology/research\\_papers/pdf/molllaserresistanceof.pdf](http://www.corning.com/discovery_center/science__technology/research_papers/pdf/molllaserresistanceof.pdf)